Corrosion Science 187 (2021) 109525

Contents lists available at ScienceDirect

Corrosion Science

journal homepage: www.elsevier.com/locate/corsci

Chromium coatings from trivalent chromium plating baths: Characterization and cathodic delamination behaviour

J. Manoj Prabhakar [a,*], Rama Srinivas Varanasi [a], Cauê Corrêa da Silva [a], Saba [a], Arnoud de Vooys [b], Andreas Erbe [a,c], Michael Rohwerder [a]

[a] Max-Planck-Institut für Eisenforschung GmbH, Max-Planck-Str. 1, D-40237, Düsseldorf, Germany
[b] Tata Steel, Research & Development, IJmuiden Technology Centre, P.O.Box 10.000, 1970CA, Ijmuiden, The Netherlands
[c] Department of Materials Science and Engineering, Norges teknisk-naturvitenskaplige universitet, N-7491, Trondheim, Norway

ARTICLE INFO

Keywords:
Trivalent chromium
Amorphous chromium oxide
Oxygen-deficient chromium oxide
Scanning Kelvin probe (SKP)
Cathodic delamination

ABSTRACT

Novel two-layer chromium-based coatings comprised of a first layer containing chromium, oxygen and carbon (Cr-O-C) and an oxygen rich (Cr-O) topcoat were electrodeposited from trivalent chromium electrolyte. The complex structure and composition of the coatings were studied using complementary characterization techniques. The electrodeposited oxide was found to be amorphous and oxygen-deficient. *In operando* ambient pressure X-ray photoelectron spectroscopy when heating the sample from room temperature to 450 °C and Raman spectroscopy after the heating ascertained the metastable nature of the oxide. The cathodic delamination of a weak model polymer on these samples was studied using *in situ* scanning Kelvin probe.

1. Introduction

Chromium-based coatings are of great importance because of their ability to protect the substrate against wear and corrosion [1]. Up to recently, the widely used standard electrodeposition process to deposit chromium utilized a hexavalent chromium (Cr^{6+}) containing electrolyte, which is now phased out from manufacturing processes, *e.g.* due to the REACH regulations in the EU [2]. Several other methods of chromium deposition were investigated previously to replace the electrodeposition from the Cr^{6+} electrolyte, such as physical vapor deposition [3,4] and electrodeposition from various trivalent chromium (Cr^{3+}) containing electrolytes [5–8]. Electrodeposition from Cr^{6+} electrolytes occurs readily on the surface of the cathode, due to the high activity of Cr^{6+}, resulting in a uniform deposit [9]. Electrodeposition from an electrolyte containing Cr^{3+} ions is more complicated than that from the Cr^{6+} electrolyte. This is because of the tendency of Cr^{3+} ions to form kinetically inert hexaqua coordinated complex $[Cr(H_2O)_6]^{3+}$ in aqueous solutions [1,10]. Hence, the reduction of Cr^{3+} to Cr is accompanied by significant hydrogen evolution as a concurrent cathodic reaction, due to the highly negative standard reduction potential associated with the process [10,11]. The rapid evolution of hydrogen results in reduced faradaic efficiency of the deposition process and also leads to increased pH resulting in precipitation of hydroxides. To overcome these complications, a complexing agent is usually used to destabilize the kinetically inert hexaqua complex and a buffering agent is used to reduce the fluctuations in pH [1,10]. The oxidation of Cr^{3+} ions in the electrolyte to Cr^{6+} during the process is avoided using an appropriate anode material [1,12] and additives such as KBr [7]. The complex mechanism involved in this electrodeposition process also results in a complicated structure of the electrodeposit, like formation of bridged complexes [1,10].

Electrodeposition from a Cr^{3+} electrolyte containing formate ions as complexing agent was found to result in a mixed Chromium-oxygen-carbon (Cr-O-C) coating [7]. The electrodeposition from the formate bath was carried out without addition of a buffering agent, thus involving the hydroxide formation as a part of the deposition mechanism [7]. These chromium-based coatings are covered by a polymer coating before application in the packaging industry [9]. Therefore, the delamination behaviour of the polymer coatings is of particular importance apart from the protection of the substrate from corrosion. Previous studies on cathodic delamination behaviour of electrodeposited chromium-based coatings demonstrated that a higher chromium oxide content in the coating leads to lower cathodic delamination rate [3,13]. It was proposed that this might be due to an increased inhibition of electron transfer to oxygen diffused to the interface by the chromium oxide. In view of this positive influence of chromium oxide in the

* Corresponding author.
E-mail address: m.prabhakar@mpie.de (J.M. Prabhakar).

https://doi.org/10.1016/j.corsci.2021.109525
Received 10 March 2021; Received in revised form 26 April 2021; Accepted 30 April 2021
Available online 4 May 2021

coating, a new concept for further improvement was to overcoat the existing Cr-O-C coatings by a Cr-O rich layer [12]. The Cr-O-C layer consists mainly of metallic chromium, whereas the Cr-O layer is oxide-rich. During the second step of the deposition at a higher current density, the enhanced hydrogen evolution leads to increased pH, resulting in the deposition of oxide [12]. The present study analyses the structure, chemical composition and cathodic delamination behaviour of these two-layers coatings and compares the cathodic delamination performance of these coatings with the traditional electrolytic chromium coated steel (ECCS), which is produced from a hexavalent chromium electrolyte. The chromium layer in the ECCS is crystalline with similar crystallographic orientation to the underlying steel substrate, and is 15−30 nm thick [14]. The coating properties are also compared with a pure chromium with native oxide layer.

Knowledge of structure and composition of the coatings is essential to ascertain their influence on the corrosion and cathodic delamination behaviour of the coatings. Compositional analysis of the Cr-O-C first layer has been carried out previously using X-ray fluorescence (XRF) and X-ray photoelectron spectroscopy (XPS) [7,13]. A detailed structural characterization of Cr-O-C coatings electrodeposited from trivalent chromium formate electrolyte has not been carried out before. Therefore, in the current study, the focus was on the investigation of the structure and composition of these coatings. High resolution transmission electron microscopy (HR-TEM) - phase contrast imaging has been employed to investigate the structure of the Cr-O-C and Cr-O nano-layers. The chemical composition of the coating at a sub-nanometre scale was investigated using atom probe tomography (APT). The chemical environment or bonding between the atoms in the samples was studied using XPS, Auger electron spectroscopy (AES) and Raman spectroscopy. The difficulties in analysing XPS data due to overlapping peaks and the assumptions needed regarding the stoichiometry of oxide and carbide to obtain the final results were discussed previously [9]. Therefore, AES and Raman spectroscopy were additionally carried out to study the Cr-C and Cr-O bonding, respectively. Ambient pressure X-ray photoelectron spectroscopy (AP-XPS), while heating the sample from room temperature to 450 °C in the presence of oxygen, was carried out to study the stability of the oxide layer.

The cathodic delamination behaviour of these two-layer chromium-based coatings with varying thicknesses of Cr-O top layer was investigated by maintaining a constant thickness of 10 nm for the Cr-O-C layer underneath. The results of the delamination studies were also compared with that of ECCS, a pure chromium sample with a native oxide and a Cr-O-C sample without the Cr-O top layer. Cathodic delamination studies were carried out using the *in situ* scanning Kelvin probe (SKP) technique [15–22]. Details of the fundamental working principle and description of the SKP used in this work can be found elsewhere [23–25]. The SKP, when accordingly calibrated, measures the electrode potential of the surface beneath the polymer [24–26]. The evolution of electrode potentials with time, across the sample, can be recorded and the rate at which the polymer delamination occurs can thus be calculated.

2. Experimental methods

2.1. Electrodeposition of chromium-based coatings on steel using trivalent chromium-coating technology (TCCT)

Samples of two-layered (Cr-O-C and Cr-O) chromium-based coatings of varying thickness of Cr-O layer, ECCS and the single-layered Cr-O-C coating were obtained from Tata Steel Packaging Europe. The electroplating was carried out in an industrial pilot coating line. The process parameters and bath composition used to obtain the coatings are described elsewhere [12]. To summarize, the Cr-O-C layer is formed in the first step during the electrodeposition process from a formate bath, and the Cr-O rich layer is formed in the second step at a higher current density. The Cr-O-C coating thickness was maintained at 10 nm for all the samples with the Cr-O topcoat. The sample without Cr-O layer had Cr-O-C layer thickness of 32 nm. Table 1 shows the different trivalent chromium coated samples used in this study and their coating thicknesses. The coating thicknesses were obtained using XPS sputter depth profile, after calculating the sputter rate by correlating the thickness measured in TEM on 2 different samples in cross section. Sample 32C which is a single step Cr-O-C coating without the Cr-O topcoat is similar to the one used in previous studies [7,13]. Pure chromium foils of 0.5 mm thickness and 99.99 % purity were procured from Goodfellow, Germany. Samples of chromium coating electrodeposited from hexavalent chromium electrolyte (ECCS) were also obtained from Tata Steel Packaging Europe. The Cr-O layer in the sample 10C-12O and the Cr-O-C layer in the sample 32C were characterized using APT, XPS, AES and Raman spectroscopy. The influence of the Cr-O layer thickness on the surface coverage was studied on the thickest (10C-12O) and the thinnest (10C-1.5O) Cr-O layered sample, using TEM. AP-XPS studies were carried out on the sample 10C-12O. The cathodic delamination behaviour of a polymer topcoat was studied on the ECCS, native oxide on chromium and all the TCCT samples mentioned in Table 1.

2.2. Characterization of chromium-based coatings

2.2.1. TEM and APT studies

Sample preparation for the TEM and APT studies was carried out using focused ion beam (FIB) milling. To prevent the coating from being exposed to the ion beam, the samples were coated with 500 nm nickel layer using physical vapor deposition (PVD). Specimens for both APT and TEM studies were prepared using a FEI Helios Nanolab 600i dual-beam scanning-electron microscope (SEM) - focused ion beam (FIB) with a Ga source. To ensure that the Ga ion beam doesn't induce structural changes in the FIB TEM cross-sectional lamella, the lamella was finally polished with a low energy beam (2 kV for 20 min.). Standard lift out protocol was employed for APT [27] and TEM [28] sample preparation.

Image-corrected FEI Titan Themis 80 − 300 (Thermo Fischer Scientific) TEM under negative Cs (−15 μm) conditions was used for HRTEM imaging by using an accelerating voltage of 300 kV.

APT data were acquired using a Cameca LEAP 5000 XR at 60 K in laser-assisted pulsing mode with 40 pJ pulse energy, pulse frequency of 1.25 kHz, at detection rates between 1–1.5 %. The data were reconstructed using Cameca's IVAS 3.8.4. The reflectron equipped LEAP 5000 XR employed in the current work leads to further enhanced mass resolution [29,30].

2.2.2. XPS and AES studies

XPS spectra were acquired with a Physical Electronics PHI Quantera II spectrometer using Al-K_α source at 1486.6 eV. Pass energy was set at 26 eV to record the core level spectra of oxygen (O 1s), carbon (C 1s), and chromium (Cr 2p). A pass energy of 59 eV was used during the acquisition of the survey scan spectra. All the measurements were recorded using a take-off angle of 45°. Energy step size of 0.025 eV was used for all high-resolution core level spectra (Cr 2p, O 1s, and C 1s), and 0.25 eV was used to collect the survey scan spectrum. The peak fitting of the core spectra obtained during the XPS and AP-XPS studies was carried out in CasaXPS software version 2.3.22. A Shirley type background was used for all the analysed spectra. Gaussian (70 %) - Lorentzian (30 %) peak shape was used for all symmetric components, and the metallic

Table 1
Details of the trivalent chromium-based coatings used in the study.

Sample code	Cr-O-C layer thickness (nm)	Cr-O layer thickness (nm)
10C-1.5O	10	1.5
10C-3O	10	3
10C-6O	10	6
10C-12O	10	12
32C	32	–

chromium component was fit using LA(1.3,4,5) peak shape to fit the asymmetric metallic peak [31]. The Cr 2p3/2 peak was fit using three components [7]: a metallic peak at ~574 eV, an oxide peak at ~575.5 eV, and a hydroxide peak at ~577 eV. A carbide peak at ~ 282 eV and an organic carbon peak at ~ 284 eV were used to deconvolute the C 1s spectrum [7]. The O 1s peaks obtained from XPS and AP-XPS studies were fit using an oxide peak at ~ 529 eV, a hydroxide component at ~ 531.5 eV and an organic oxygen/water peak at ~ 533 eV [7].

Auger spectra were obtained using a JEOL JAMP 9500-F scanning Auger microprobe. The spectra were differentiated and plotted in CasaXPS software version 2.3.22. AES was used to ascertain the chemical environment of carbon in the coatings.

2.2.3. Raman spectroscopy of as-deposited and heat-treated TCCT

Raman spectra were recorded with a WiTec Alpha 300 M confocal Raman microscope. A laser with an excitation wavelength of 532 nm was used. The spectra were recorded in an ambient air atmosphere using the 100X magnification objective of the microscope. The resulting spectra were analysed using WiTec Project FIVE software. Raman spectra were recorded from different regions of the sample to verify the repeatability of the measurements. Surface maps obtained using the same instrument were processed in WiTec Project FIVE to correct background and remove cosmic rays. Non-negative matrix factorization as implemented in the control software was carried out to unmix spatial distribution of various components in the maps.

2.2.4. AP-XPS studies

AP-XPS measurements were carried out in a PHOIBOS 150 NAP 2D DLD hemispherical energy analyser customized equipment (SPECS Surface Nano Analysis GmbH). Metal stripes were screwed to attach the sample to the sample holder and a thermocouple type K was point welded to one of the stripes, on a spot above the sample, to read the temperature of the sample during *in situ* heating with an infrared laser. The sample was heated from room temperature to 450 °C at 50 °C intervals. To characterize the coating at different temperature, *in situ* XPS spectra were obtained during heating, with an incident photon beam of energy 1486.7 eV corresponding to the Al-K_α emission line. All the spectra were obtained with a pass energy of 40 eV and a step size of 0.5 eV. A dwell time of 0.2 s was used in all the measurements. The heating and XPS measurements were carried out in an atmosphere of 1 mbar of O_2.

In the equipment used for the studies, a small NAP (near ambient pressure) reaction chamber is driven into the analysis chamber. Gas is allowed to flow through the NAP cell resulting in a defined pressure inside it. The NAP cell offers the advantage of requiring a smaller gas flow than what would be necessary to fill the whole analysis chamber, thus also enabling a quicker gas exchange and reducing the time required for preparation of the experiment.

2.3. SKP measurements

To carry out cathodic delamination measurements with SKP, the chromium coated steel samples or pure chromium samples were cut into sheets of dimension 20 mm x 20 mm. The sheets were then coated with 10 wt.% PVB polymer in ethanol, in a spin coater. The polymer-coated sample was placed in contact with 1 M KCl reservoir on a steel plate. The reservoir was constructed on the steel plate by using X60 cold curing adhesive to form the walls of the reservoir and placed adjacent to the polymer-coated sample as illustrated in Fig. 1. The setup containing the polymer-coated sample and the reservoir was placed in the SKP to carry out delamination measurements. All the measurements were carried out in air, at high relative humidity (RH > 93 %) and room temperature. Before each experiment, the Ni-Cr SKP tip was calibrated against Cu/$CuSO_4$ standard electrode, and the corrosion potential measurements were recorded with respect to standard hydrogen electrode (SHE) after the calibration.

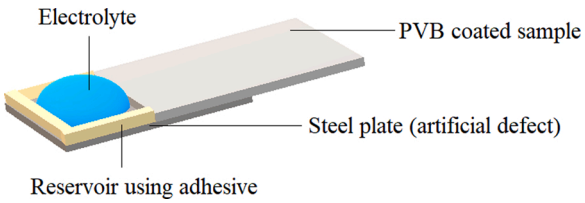

Fig. 1. Schematic of the sample prepared for cathodic delamination studies.

3. Results

3.1. Structural characterization

Fig. 2a shows the high-resolution TEM micrograph of the cross-section of a 10C-12O two-layer sample with the thickest Cr-O layer. The TEM micrograph is depicting the 12 nm Cr-O layer and 10 nm Cr-O-C layer sandwiched between the nickel coating and the steel substrate. As mentioned in section 2.2.1, the 500 nm of Ni coating just served to prevent damage to the coating during FIB milling. Diffraction spots in the diffraction pattern of the sample (shown in Fig. 2b, inset) indicate the [113] crystallographic orientation of the grains in the steel substrate. The TEM micrograph shows no uniform periodic arrangement,

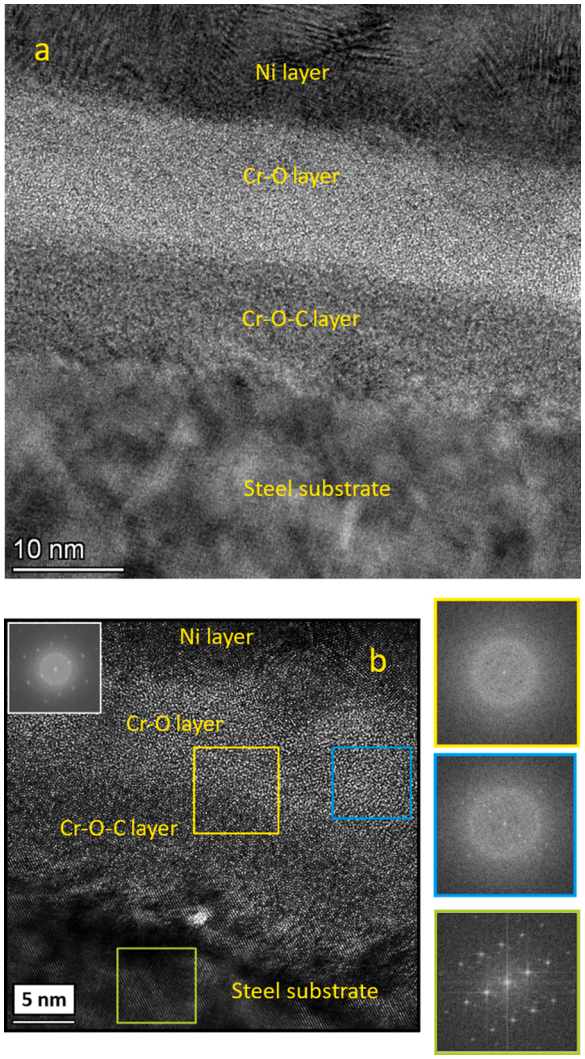

Fig. 2. a) TEM micrograph of the cross-section of the 10C-12O sample and b) Fast Fourier transformations from various locations on the 10C-12O sample (coloured boxes).

indicating the strongly disordered nature of both the chromium layers. This was further verified from the diffraction patterns obtained using fast Fourier transformation (FFT). Diffuse rings or the absence of diffraction spots in the FFTs of different regions of the chromium layers, indicated by the respective coloured boxes in Fig. 2b, reaffirm the amorphous nature of both the layers.

Fig. 3a depicts the HR-TEM image of the cross-section of a 10C-1.5O sample, which has a metallic Cr-O-C layer of 10 nm thickness and Cr-O layer of 1.5 nm thickness. This much thinner Cr-O layer is not homogeneous across the surface, and a thicker layer is formed at certain locations (highlighted with a red box in Fig. 3a). Fast Fourier transformations on these thick locations reveal ordering (crystalline native oxide in Fig. 3b).

3.2. Chemical composition analysis

The sample types 10C-12O (Fig. 4a) and 32C (Fig. 4c) were also analysed using APT. One dimensional (1D) compositional profiles with a bin width of 0.3 nm (Fig. 4b & d) were obtained by placing a cylindrical region of interest (ROI) of diameter 10 nm across the coating as shown in Fig. 4a & c. The distance in the x-axis (Fig. 4b & d), increases along the direction of the black arrow marked in Fig. 4a & c.

Fig. 4a & c depict the distribution of Cr & O in the Cr-O layer and Cr, O & C in the Cr-O-C layer, respectively. As expected from the

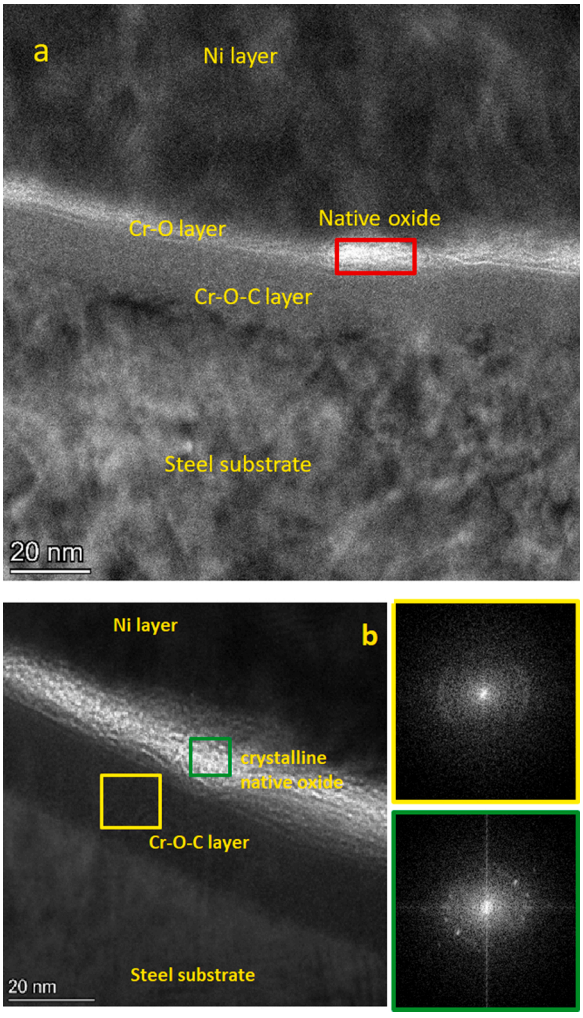

Fig. 3. a) TEM micrograph of the cross-section of the 10C-1.5O sample depicting native oxide formation (red box) and b) Fast Fourier transformations from the amorphous Cr-O-C layer (yellow box) and native oxide (green box) on the 10C-1.5O sample.

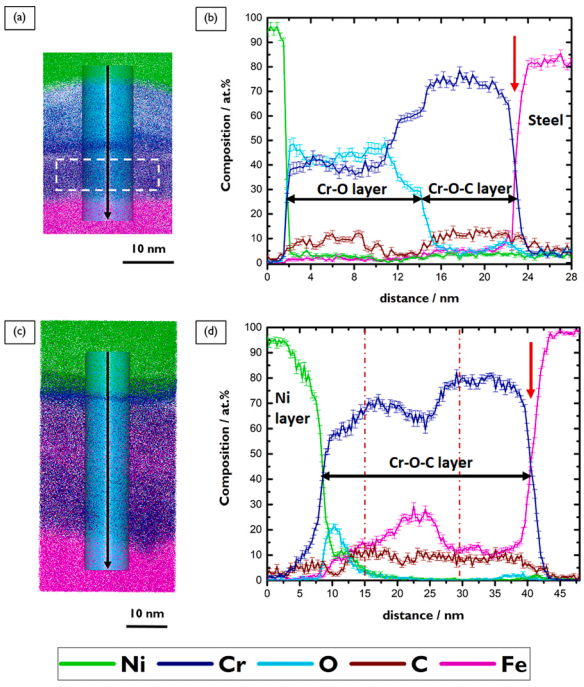

Fig. 4. (a) Three-dimensional APT result of sample 10C-12O, (c) Three-dimensional APT result of sample 32C, (b) and (d) 1-D elemental profile across the coating for the cylindrical ROIs in (a) and (c) respectively.

electrodeposition process, the amount of oxygen is much higher in the Cr-O layer than in the Cr-O-C layer, and carbon incorporation in the coating is eliminated in the second step of electrodeposition at a higher current density [12]. From the 1D composition profiles in Fig. 4b & d, it is evident that the Cr and O are not present in a stoichiometric ratio that would be expected for chromium oxides (2:3 for Cr_2O_3 or 1:2 for CrOOH), but rather in a 1:1 ratio. The amorphous oxide is therefore oxygen-deficient, compared to stable oxides or oxy-hydroxides of chromium, and will henceforth be referred to as metastable oxide. The 1D compositional profiles also reveal the presence of oxides at the interface between the steel and the Cr-O-C layer (marked by red arrows in Fig. 4b & d).

Moody et al. [32] reported that the Pearson coefficient μ is a robust parameter to detect any solute segregation in atom probe datasets. A Pearson coefficient value of 0 indicates a random distribution, while the value of 1 signifies the segregation of the solute atoms. To affirm the homogeneity of C in the Cr-O-C layer, the Pearson coefficient μ was calculated from the 100-atom bin size frequency distribution analysis within a cuboidal ROI of dimensions 20 × 20 × 7 nm^3 (as shown with white dotted lines in Fig. 4a). The carbon has a Pearson coefficient value of 0.021, which indicates the homogenous distribution of carbon atoms in the Cr-O-C layer. Also, the stoichiometry of Cr:C is not close to any stable carbide of chromium. Similar analysis on the sample 32C in Fig. 4c resulted in a Pearson coefficient value of 0.038 for carbon. The 1-D compositional profile indicates some Fe enrichment in the Cr-O-C layer (red dotted lines in Fig. 4d). Fe enrichment in the Cr-O-C layer of the sample 10C-12O can also be observed from the higher amount of Fe in the Cr-O-C layer than the Cr-O layer (Fig. 4b). This can be attributed to the codeposition of Fe arising due to dissolution and redeposition occurring during the chromium electrodeposition process from trivalent chromium electrolyte [9,13].

3.3. Chemical state analysis

3.3.1. XPS and AES

XPS analysis of amorphous, oxygen-deficient oxide is associated with peak shifts for each oxidation state compared to their crystalline

counterparts [33]. This is attributed to the changes in metal-oxygen bond distances and coordination number of the metal atoms in an amorphous phase. This could lead to an erroneous association of peak positions, especially in metals which can occur in more than one oxidation state. Hence, in the current work, emphasis was given to a careful qualitative analysis of the obtained XPS spectra. The survey scan spectra from XPS revealed that the sample 32C without the Cr-O layer contains a higher amount of carbon compared to 10C-12O, which has a 12 nm Cr-O topcoat (Fig. A1). Also, the amount of oxygen on the Cr-O layered 10C-12O is higher compared to 32C, as expected.

Fig. 5a depicts the Cr 2p spectrum of the samples 10C-12O and 32C. The Cr $2p_{3/2}$ peaks of the samples were fitted for chromium in metallic, oxide, and hydroxide chemical environments (Fig. A2). The 32C sample is composed of a considerable amount of metallic Cr just below the native oxide, depicted by the clear asymmetric metallic peak. The metallic peak is completely absent in the Cr-O layered 10C-12O sample ascertaining that all Cr atoms are present in oxide or hydroxide environment. This was also ascertained by carrying out XPS depth profiling of the 10C-12O sample, and it was found that the Cr atoms throughout the Cr-O layer were present in an oxide or hydroxide environment (Fig. 6). The depths depicted in Fig. 6 are obtained after calibrating the sputter depth in XPS with the thickness obtained from HR-TEM. Also, the absence of chromium in an organic carbonyl group environment can be ascertained by the absence of satellite peaks in the Cr 2p spectrum. The satellite peaks are characteristic of the interaction between chromium and carbon in C═O environment [34,35].

The O 1s spectra obtained from the samples were fit using peaks for oxide and hydroxide/defective oxide (Fig. A3). XPS peak fitting of oxides and defective oxides has been carried out previously, following a similar procedure [31,36,37]. According to this evaluation, oxygen in the 10C-12O sample seems to be mainly in a defective oxide or hydroxide environment, whereas the 32C sample seems to be composed of a higher fraction of oxide than defective oxide or hydroxide (Fig. 5b). It should be noted that the XPS O1 s spectrum of the 10C-12O sample reveals a very low oxygen content in the oxide environment compared to the 32C sample, *i.e.* typical native oxide layer is absent here. This chromium oxide of 1:1 Cr:O ratio should thermodynamically not be stable, but as it seems to exhibit an extremely low reactivity with the ambient atmosphere, it has to be metastable.

The C 1s spectra in Fig. 5c show that the sample 32C contains a certain amount of C in a carbide environment, which is absent in the Cr-O layer of the sample 10C-12O. The peak fitting of the carbon peaks is shown in Fig. A4. The sample 32C consists of C in both aliphatic carbon environment (C-C and C–H) and carbide environment (Cr-C), whereas the Cr-O top layer of the sample 10C-12O contains carbon only in aliphatic carbon environment. Even though the C 1s spectrum shows the presence of organic/aliphatic carbon on the sample, the amount of C on the surface of 10C-12O is much lower compared to the 32C sample, as observed from the XPS survey scan (Fig. A1).

To ascertain the presence of carbon in a metal carbide environment, Auger electron spectroscopy was carried out on both the Cr-O and Cr-O-C layers. The derivative Auger spectra corresponding to C KVV energies are shown in Fig. 7. The line shape observed in the 10C-12O sample (Fig. 7a) corresponds to that of carbon in graphitic carbon, whereas that in sample 32C (Fig. 7b) depicts carbon in metal carbide environment [38,39].

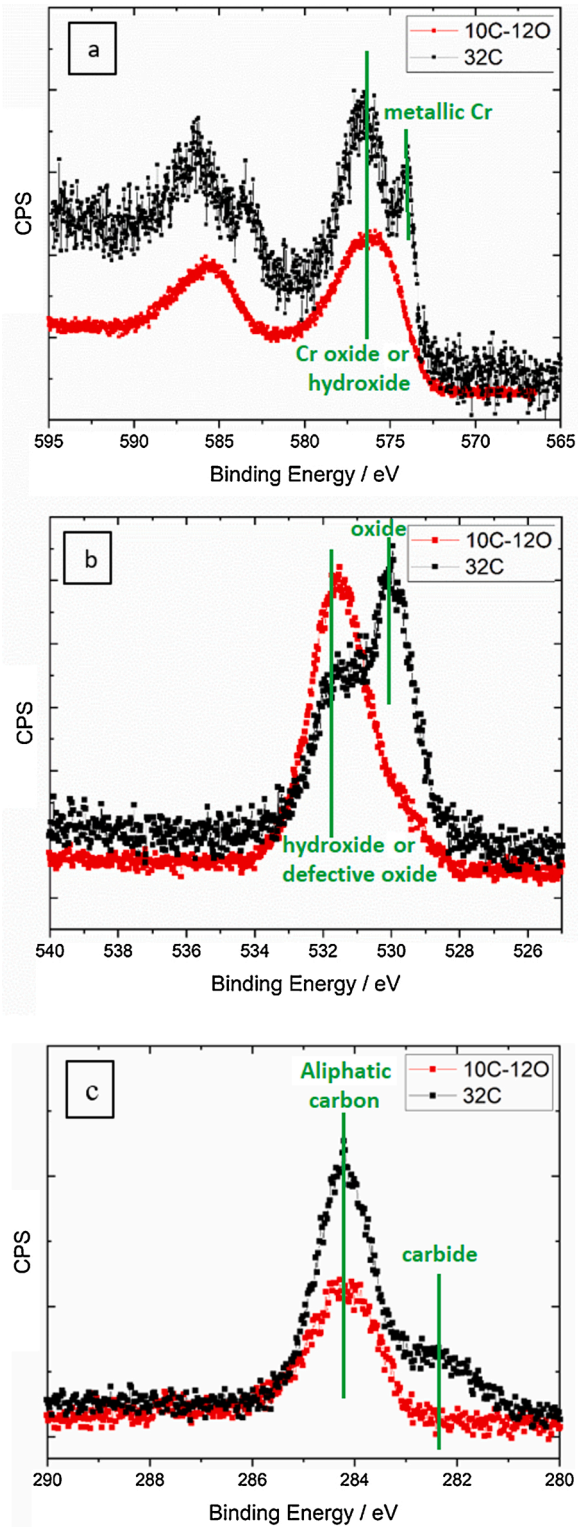

Fig. 5. Core level spectra of samples 10C-12O and 32C a) Cr 2p, b) O 1s and c) C 1s.

3.3.2. *Raman spectroscopy*

Raman spectra were measured on samples 10C-12O and 32C to further study the nature of the Cr-O, and Cr-O-C coated surface. Fig. 8 depicts the different regions of the spectrum obtained from the samples. Both the samples exhibit similar Raman shifts in the regions 150 cm^{-1} to 750 cm^{-1} and 1000 cm^{-1} to 1700 cm^{-1}, as can be seen in Fig. 8 a & b. Peaks at ~ 222 cm^{-1}, 285 cm^{-1}, 400 cm^{-1}, 600 and 650 cm^{-1} were observed in the region with characteristic oxide peaks. Fe_2O_3 has peaks around all of these wavenumbers, with some variations [40–43]. *Via* the absence of a significant peak in the region around 3400 cm^{-1}, the presence of significant amounts of hydroxide can be ruled out [44]. A Raman shift at 550 cm^{-1} corresponding to the A_{1g} mode of crystalline α-Cr_2O_3 [44–47] was absent in both the samples, which may be a sign of the effect of disorder.

In the region 1000 cm^{-1} to 1700 cm^{-1}, the Raman shift at ~1350 cm^{-1} and 1580 cm^{-1} depict the D and G band, respectively, of

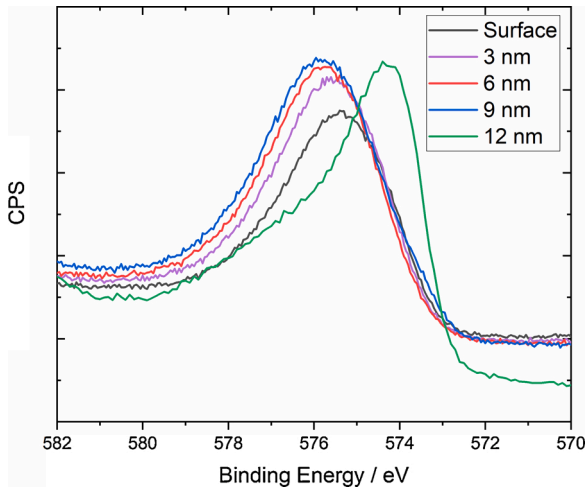

Fig. 6. Cr 2p3/2 spectra obtained from sample 10C-12O at various depths.

predominantly sp^2 carbon [48,49]. The D band at ~1350 cm^{-1} arises in the presence of disorder in graphite [50]. The G band at ~1580 cm^{-1} is due to bond-stretching of a pair of sp^2 carbon atoms and is not specific to ring structures. The intensity ratio between the D and G peak, *I(D)/I(G)*, is of interest here since both samples exhibit a peak at similar wavenumbers but differ in the intensity ratio (Fig. 8b). This ratio is a measure of the number of defects in a graphitic structure [51,52]. The number of defects in the graphitic domains in the sample 10C-12O is thus significantly higher than in the sample 32C. The width of the peaks indicates that, especially in the sample 10C-12O, the sp^2 carbon is close to amorphous.

As depicted in Fig. 8c, the major difference between the samples 10C-12O and 32C was observed in Raman shifts in the region 2650 cm^{-1} to 3050 cm^{-1}. In this region, the 2D peaks of graphitic structures are observed below 2800 cm^{-1} [50], and CH stretching modes of hydrocarbons usually above 2800 cm^{-1} [53,54]. The peaks at ~ 2850 cm^{-1} and 2890 cm^{-1} are typically assigned to symmetric stretching modes of CH_2 and CH_3 groups, respectively, in long aliphatic chains [54]. Components at ~2930 cm^{-1} and 2960 cm^{-1} correspond to antisymmetric stretching modes of CH_2 groups and an asymmetric stretching of a CH_3 group, respectively [53].

Raman spectroscopic mapping (Fig. 9) shows that the organic (green) component, the sp^2 carbon (blue) component and the oxide (red) component are not always co-located. The different colours corresponding to different components were obtained using non-negative matrix factorization of the Raman spectroscopic maps. Non-negative matrix factorization has been used previously to unmix complex Raman spectroscopic maps [55,56]. The layers do, therefore, have some lateral structure at the microscopic scale. However, the absence of any heterogeneity or particles in the TEM, implies that these heterogeneities arise due to fluctuations in the amorphous structure. At a nanoscopic scale and small sampling volumes processed in APT, uniform distribution of carbon is observed. The detailed investigation of this lateral structure and its possible relation to the substrate is beyond the scope of this work.

3.3.3. *Restructuring on heating*

From the XPS spectra in Fig. 5b, the Cr-O layer was observed to be unreactive with the ambient atmosphere. The layer was therefore inferred to be a metastable oxide. To confirm the metastable nature of the oxide in the Cr-O layer, the sample 10C-12O with the thickest Cr-O layer was heat-treated from 25 °C to 450 °C at 50 °C intervals in the presence of 1 mbar O_2. The applied heating was maintained constant for a duration of 40 min, during which *in situ* XPS measurements were carried out. The XPS spectrum showed no observable difference from room temperature to 250 °C. The evolution of O 1s XPS spectrum with increasing temperature is shown in Fig. 10. It can be observed that the O 1s peak at room temperature consists of a negligible amount of stoichiometric oxide (Fig. 10a). The oxide peak grows stronger at the expense of the hydroxide / defective oxide peak (Fig. 10b) with an increase in temperature, and finally, at 450 °C, the sample is completely converted into a stoichiometric oxide with a negligible amount of hydroxide or defective oxide (Fig. 10c).

To verify the ordering transformation caused by heating in the presence of oxygen, Raman spectroscopy was carried out on the sample 10C-12O, before and after heating to 450 °C (Fig. 11). Cr_2O_3 exhibits a characteristic peak at around 550 cm^{-1}, which corresponds to the A_{1g} mode involving Cr-O stretching in octahedrally O-coordinated Cr^{3+} of Cr_2O_3 [45–47], and can be seen in the native oxide formed on pure chromium in Fig. 11. It is evident from the spectra in Fig. 11 that the peak is absent in the as-deposited Cr-O layer indicating the absence of this oxide. The stoichiometric chromium oxide is formed after heating to 450 °C, manifested by the appearance of the peak at 550 cm^{-1}. This further validates the defective nature of the oxide in the as-deposited coating.

3.4. *Cathodic delamination studies*

The corrosion potential (E) *vs.* distance from the defect boundary plots of PVB as weak model coating, measured for the samples 32C,10C-1.5O, 10C-3O, 10C-6O, 10C-12O, pure chromium with native oxide and ECCS are presented in Fig. 13. The point of inflection in the E *vs.* distance to defect curve is considered to be the position of the delamination front [16] and the rate of change of this position with time is used to calculate the rate of delamination of the polymer coating. The position at a corrosion potential of 50 mV (average of the potentials between the cathodic and anodic regions) was considered as position of the delamination front for Fig. 13g, owing to difficulties in finding the point of inflection in these curves. The delamination rate of the polymer coating was determined by plotting the position of the delamination front with

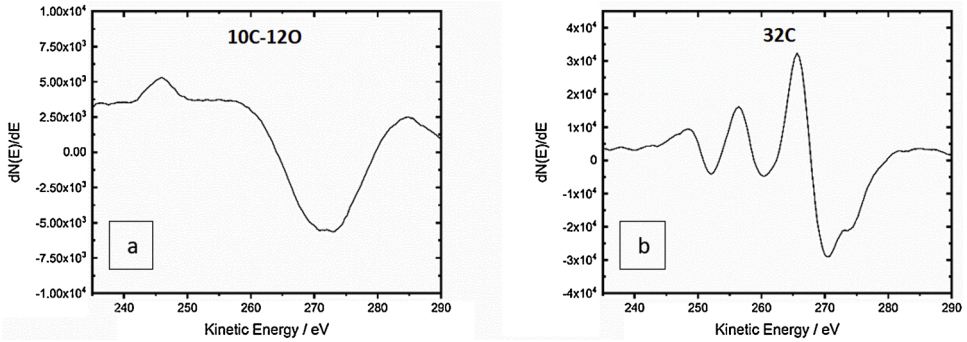

Fig. 7. C KVV Auger spectra of sample a) 10C-12O b) 32C.

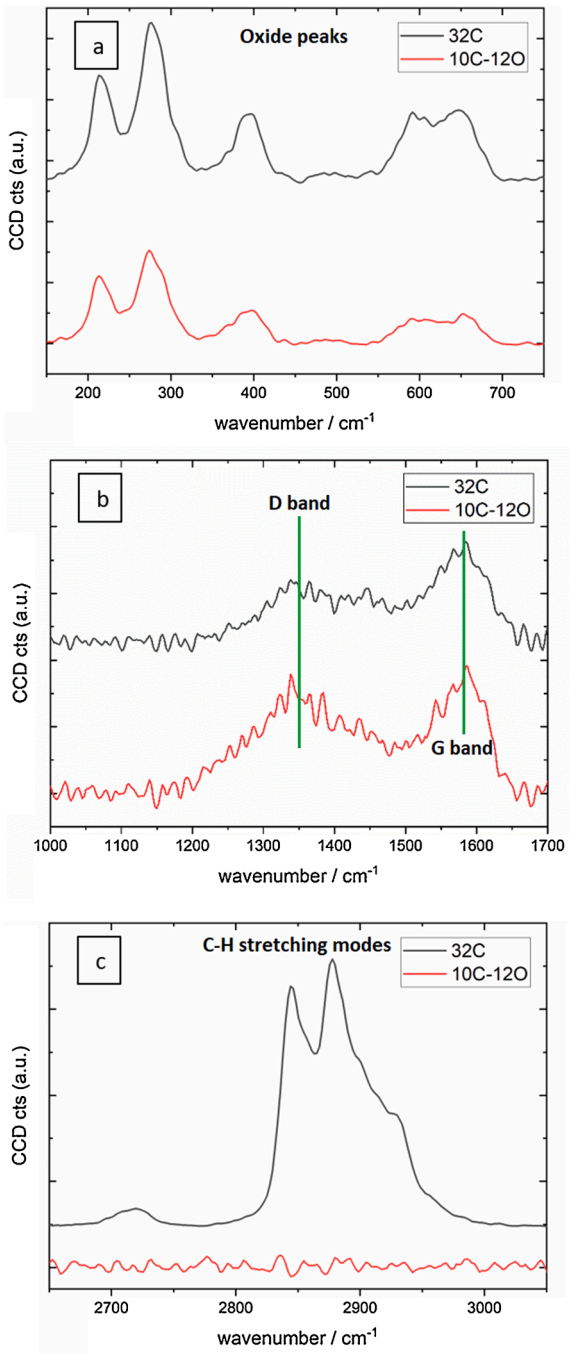

Fig. 8. Raman spectrum from samples 10C-12O (Cr-O-C and Cr-O) and 32C (Cr-O-C) depicting the wavenumber regions of Raman shift a) 150 to 750 cm^{-1} b) 1000 to 1700 cm^{-1} c) 2650 to 3050 cm^{-1}.

time and evaluating the slope of the resulting curve. The position of the delamination front with time for various samples used in this study are shown in Fig. 14a & b. The curves were fit using linear ($x_{del} = x_i + a{\cdot}t$) and sqrt(t) models ($x_{del} = x_i + a{\cdot}\sqrt{t}$) and the quality of the fits were evaluated using the correlation coefficient (R^2) values for each of the fits. Linear and sqrt(t) models were used to demonstrate whether the delamination kinetics was dominated by the electron transfer or the cation migration, respectively. Table 2 summarizes the rates obtained on fitting the delaminated distance *vs.* time plots of different samples and their correlation coefficients.

As summarized in Table 2, the delamination rate of 10 wt.% PVB coated on traditional ECCS sample assuming a linear delamination kinetics was found to be 42 μm/h. However, fitting with a sqrt(t) function was found to yield better results as observed from the R^2 values for the linear fit. The rates of delamination on the 10C-1.5O, 32C and the pure Cr with native oxide samples were found to be quite similar as depicted in Fig. 14a and Table 2. All these three samples were found to predominantly follow sqrt(t) kinetics, as revealed from their better R^2 ratios for a sqrt(t) fit. The samples 10C-3O, 10C-6O and 10C-12O were found to rather follow linear delamination kinetics and the delamination rate decreased with increase in the thickness of Cr-O layer as can be seen in Fig. 14b.

4. Discussion

4.1. Structural and chemical characterization

HR-TEM studies on the sample 10C-12O (Fig. 2) reveal the amorphous nature of both Cr-O and Cr-O-C layers in the sample 10C-12O. Such amorphous nature was previously observed in chromium-based coatings obtained by electrodeposition [57] and magnetron sputtering [58,59], and can be explained by the high rate of deposition employed, leading to rapid nucleation and reduced growth of nuclei. Also, chromium-carbon films are reported to be generally amorphous over a wide composition range and deposition conditions due to their high ability to form glasses [58]. The presence of a crystalline phase in the 10C-1.5O sample (Fig. 3) can be ascribed to the oxidation of metallic chromium upon the exposure of the Cr-O-C layer to the ambient atmosphere. The electrodeposited Cr-O layer seems to be unreactive with the ambient atmosphere, and prevents underlying metallic chromium from oxidation, even at lower thicknesses than that of native oxide (Fig. 3a). Correlating the APT data with TEM data, the electrodeposited Cr-O layer can be inferred as an amorphous oxide, which is deficient in oxygen. Contrary to the assumptions in earlier reports regarding the stoichiometry of the carbide and oxide [7,13,60], TEM and APT studies reveal the absence of oxide or carbide particles in both layers of the coating.

From the XPS O 1s spectra in Fig. 5b, it is evident that the oxide peak at lower binding energy is almost suppressed completely in the sample 10C-12O. The high amount of oxide on the sample 32C in Fig. 5b results from the oxidation of metallic Cr, on exposure to ambient environment after the electrodeposition process. The thin surface oxide layer can also be observed from the APT 1D composition profile of 32C sample (Fig. 4d), where the oxygen composition is higher close to the surface to a depth of ~ 5 nm. These observations in XPS and APT also ascertain the oxide layer formation observed in TEM (Fig. 3a & b), at locations where the Cr-O-C layer is exposed. In contrast, the distribution of the oxygen composition in the 10C-12O sample is uniform throughout the Cr-O layer (Fig. 4b), also close to the surface, affirming the metastable nature of the Cr-O layer.

The Auger spectra confirm the formation of metal-carbon bonds in the Cr-O-C layer and not in the Cr-O layer, as also observed in the XPS spectra. Though we observe metal-carbon bonding in XPS and AES, there are no carbide particles observed in TEM and APT. Further, the Pearson coefficient analysis reveals the uniform distribution of carbon in the layer, denoting carbon in oxycarbide and aliphatic carbon states, uniformly distributed across the layer.

The oxide peaks obtained in the Raman spectra in Fig. 8a, indicate that Fe_2O_3 is likely present at the interface between the steel and the electrodeposited Cr coating. This can also be verified from the elemental composition analysis from APT in Fig. 4b & d. A notable increase in the concentration of oxygen is observed at the interface between the steel substrate and the chromium layer (marked by red arrows in Fig. 4b & d), which results from the oxidation of the substrate. The organic carbon peaks (Fig. 8c) are completely absent in the sample 10C-12O. This observation is in line with XPS analysis, where the amount of carbon on the surface of the 32C sample is much higher than that of the 10C-12O sample. It is interesting to note the organic nature of the observed carbon. It is difficult to explain these with the typical impurities originating

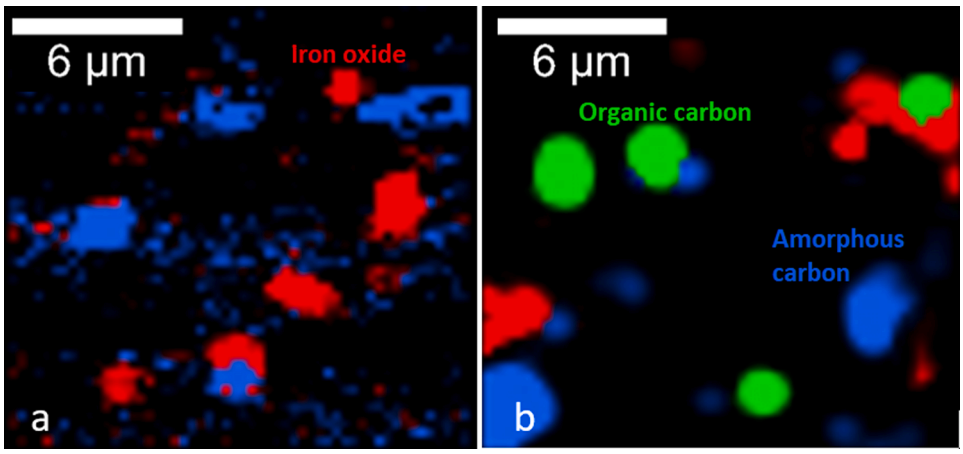

Fig. 9. Raman spectroscopic mapping of samples a) 10C-12O and b) 32C, denoting the regions of iron oxide (red), amorphous carbon (blue) and organic carbon (green).

from adsorption of organic contaminants from the atmosphere; such adsorption would not explain the differences between different samples, and would in addition, not likely be detected by Raman spectroscopy. Hence, the origin of these organic species has to be from differences in incorporation of formate ions from the electrolyte bath used for electrodeposition. The formate ions or other organic additives are reduced along with the chromium ions during the electrodeposition process and incorporated as carbon in the layers [7,11,34,57]. During the process, possibly in side reactions, organic species with CH_2 and CH_3 groups may form.

The *in situ* heating experiment in AP-XPS reveal restructuring of the oxide layer in the sample 10C-12O (Fig. 10). From Raman spectra analysis, we know that the amount of hydroxides is below detectible limits and is thus negligible. The restructuring can therefore be inferred as the transformation of a defective oxide into a stoichiometric oxide, substantiated by the appearance of the characteristic peak at 550 cm^{-1} (Fig. 11). The *in situ* heating experiment also confirms that the Cr-O layer is stable up to a temperature of 250 °C, ascertaining its metastable nature.

A correlation between the various studies here gives a holistic picture of the Cr-O-C and Cr-O layers. Chemical bonding analysis using XPS reveals that the Cr-O-C layer constitutes of chromium as metal, oxide, hydroxide or defective oxide and carbide. Organic and defect rich sp^2 carbon species are also present. The carbon atoms in the Cr-O-C layer are present in a mixture of carbide [34], aromatic and aliphatic carbon as observed in earlier studies [58,59]. However, the nature of the carbide phase was not discussed in detail before. In the present work, the absence of carbide particles in TEM and APT studies establish that the carbon is present as amorphous non-stoichiometric oxycarbide, distributed uniformly across the coating at nanoscopic scales. At microscopic scales, however, lateral inhomogeneities are observed in Raman spectroscopic mapping. Additionally, XPS and Raman spectroscopy reveal the presence of carbon as aliphatic and unsaturated carbon (C═C and C–H). Also, a higher content of organic and amorphous carbon in the Cr-O-C layer of the sample 32C was found. The oxygen atoms in the Cr-O-C layer are present in a defective oxide chemical state with a stoichiometric oxide layer formed near the surface due to the reaction of the metallic chromium with air. The hydroxide content in the layers was found to be below detectible limits from Raman spectroscopy. The deposited oxide was also found to be metastable, unreactive to the ambient atmosphere. In a nutshell, Fig. 12 illustrates the findings regarding the oxide in the layers on the samples with 1.5 nm and 12 nm Cr-O layers. No evidence for the presence of crystalline Cr_2O_3 was found before heat treatment. AP-XPS and Raman spectroscopy post-heat treatment show a transformation of the non-stoichiometric oxide into a phase with the typical octahedral coordination of Cr^{3+} by oxygen after heat treatment.

4.2. Cathodic delamination behaviour

The evolution of corrosion potential *E* during the process of delamination led to the formation of three distinct regions [15,16],

i a delaminated region; the polymer is delaminated and potential is close to that of the defect,
ii an intact metal/polymer interface region; the polymer is still intact and
iii a delamination front; a gradual change in corrosion potential and oxygen reduction occurs, which leads to degradation of the polymer at the interface with the metal and to its delamination.

The steepness of the delamination front can be considered as an aspect that indicates the extent of cation diffusion into the intact metal / polymer interface [21,61]. A sharp increase in potential at the delamination front can indicate inhibited cation migration into the intact interface. Higher rates of cation migration into the intact interface compared to the rate of oxygen reduction (or more inhibited oxygen reduction induced interfacial degradation relative to the cation migration rate) at the active front can be a plausible reason for a more gradual increase in potential at the front. It can be observed from Fig. 13f that the rate of cation migration is faster on the native oxide covered chromium, resulting in a gradually changing potential at the delamination front. It is noteworthy that on all the different TCCT used in this study, a steep change in potentials at the delamination front was observed, which can be hypothesized as an effect of hindered cation migration.

The difference in potentials between a point close to the defect and a point just before the delamination front is the ohmic drop or *iR* drop. This arises due to the ionic current *i* and the resistance to ionic current *R* between the local anode (defect) and the local cathode (delamination front) [20]. This lateral ionic current sustains the cathodic oxygen reduction reaction occurring at the delaminated interface and at the delamination front. The delamination profiles in Fig. 13 elucidate that the potential drop observed in the native oxide is much higher than those observed in TCCT. This could arise from a lower rate of oxygen reduction (lower *i*, thus lower *iR*) on the TCCT due to decreased conductivity of the metastable oxide layer compared to the native chromium oxide. Further investigation on the ohmic drops occurring in the delaminated region on these samples is beyond the scope of the current work.

In a system where the delamination rate varies linearly with the square root of time, the rate of delamination is assumed to be controlled by the cation migration from the defect (anode) to the delamination

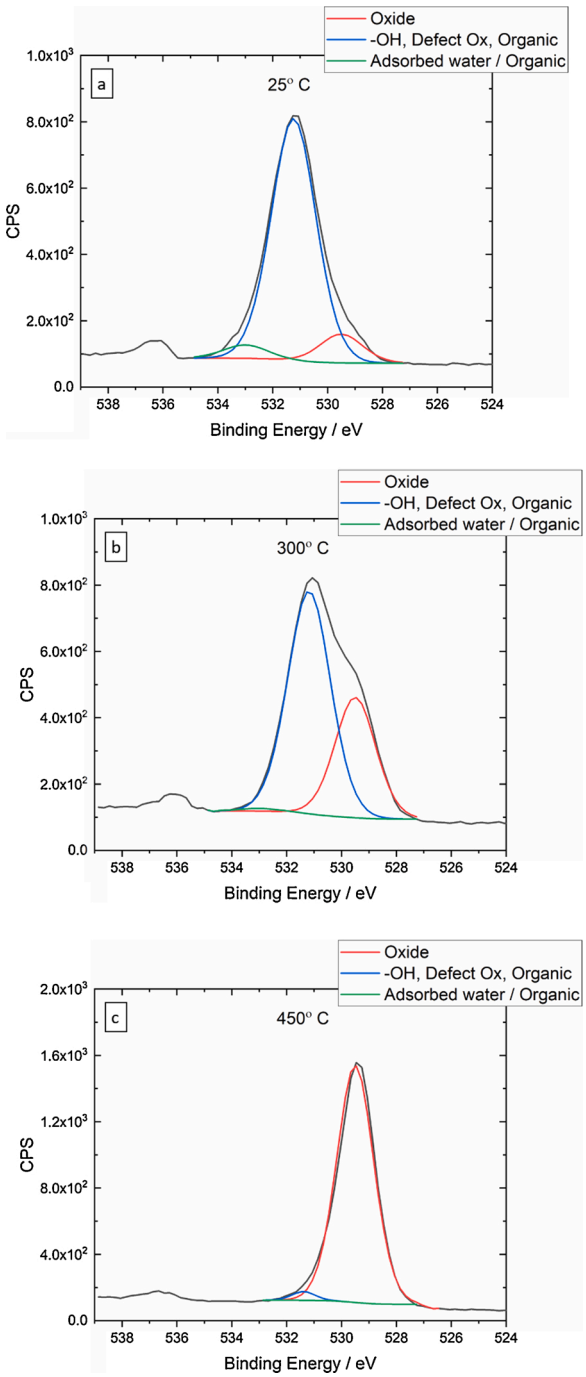

Fig. 10. XPS O 1s spectrum of sample 10C-12O acquired in 1 mbar O_2 environment at a) 25 °C b) 300 °C c) 450 °C.

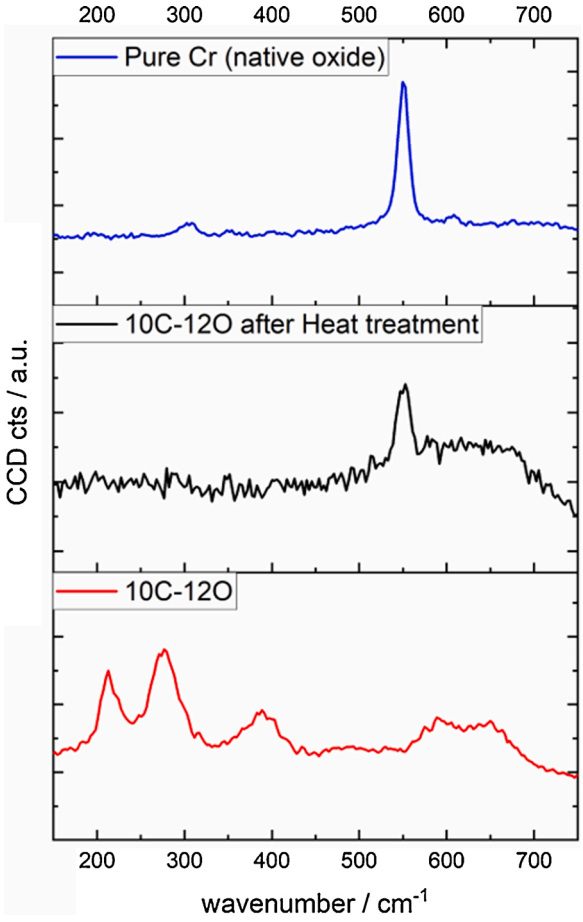

Fig. 11. Raman spectra obtained from sample 10C-12O, before and after heating to 450 °C.

Table 2
Delamination rates obtained on fitting the delamination distance *vs.* time plots in Fig. 14a & b, and the correlation coefficient (R^2) values.

	Linear fit		Sqrt(t) fit	
	Rate (μm/h)	R^2	Rate constant (μm/$h^{1/2}$)	R^2
Native oxide	828 ± 38	0.9613	3666 ± 48	0.9971
32C	827 ± 42	0.9823	3923 ± 140	0.9979
10C-1.5O	784 ± 26	0.9878	3207 ± 32	0.9993
10C-3O	415 ± 5	0.9960	2665 ± 51	0.9905
10C-6O	36.2 ± 0.3	0.9984	692 ± 10	0.9930
10C-12O	9.2 ± 0.1	0.9966	239 ± 2	0.9942
ECCS	42.1 ± 1.1	0.9508	647 ± 11	0.9828

front (cathode) [15,19]. When the electron transfer for oxygen reduction reaction is the rate-controlling process, a linear relation between the position of delamination front and time is observed [21,62]. Previous measurements on PVB coated ECCS, with a defect filled by an aqueous solution of 0.86 M NaCl, resulted in no observable delamination within 96 h [9]. This could be due to the electrolyte being in contact with ECCS in the previous study [9] where the anodic dissolution reaction is inhibited, in contrast to a steel defect in this study. This would potentially lead to a lower corrosion potential in the defect and hence to a higher driving force for delamination in this study. The delamination of PVB on ECCS in the presence of steel defect covered with 1 M KCl electrolyte (Fig. 13g), can be inferred as a possible ion migration-controlled process, from the observed sqrt(t) kinetics in this study. It should be emphasized that the potential profile observed in ECCS is distinct, that the potential in the delaminated region is not levelled and an inhomogeneous potential distribution exists, unlike in the other samples.

Albeit similar delamination rates of PVB on samples 10C-1.5O, 32C and native oxide on chromium (Fig. 14a), the cation migration most likely was faster in the native oxide compared to the other samples, as could be deduced from the shape of the delamination front. The similar delamination rates in these samples can be explained by the non-uniform coverage of the surface by the Cr-O layer in the sample 10C-1.5O as observed in TEM (Fig. 3), leading to the oxidation of underlying metallic chromium, *i.e.* the presence of areas covered by the native oxide. Similar oxidation of metallic chromium is also possible in the sample 32C.

The results indicate an electron transfer controlled delamination

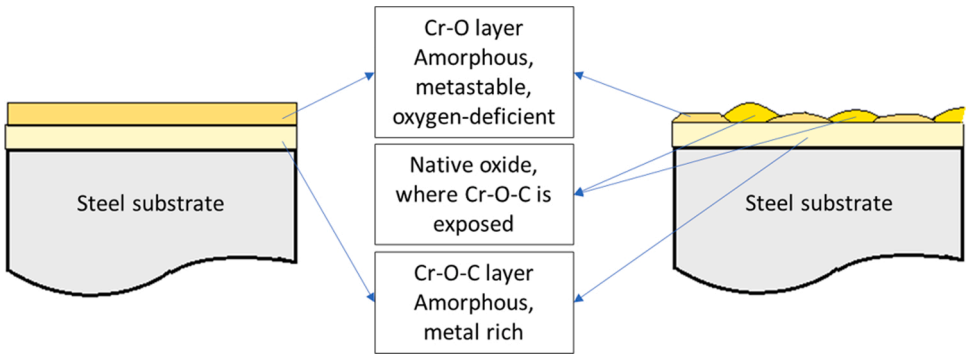

Fig. 12. Schematic depicting the novel two-layers in TCCT with 12 nm Cr-O topcoat (in the left) and 1.5 nm Cr-O topcoat (in the right).

mechanism on the samples with Cr-O layer thickness of at least 3 nm and cation migration-controlled process in 10C-1.5O, 32C and native chromium oxide samples. The metastable oxide layer plausibly hinders charge transfer for the oxygen reduction reaction to occur, thus greatly reducing the rate of delamination and displaying an electron transfer controlled delamination kinetics. Similar behaviour was also observed on native oxide of chromium, where PVB on native oxide was found to delaminate faster than ECCS [3]. From Fig. 14b and Table 2, it is evident that the ECCS and 10C-6O samples have similar rates, though the initiation time for delamination was found to be higher in the 10C-6O sample. The 10C-12O sample was found to delaminate four times slower than the ECCS sample.

Thus, the Cr-O layer has a tremendous impact on cathodic delamination behaviour. Though the total coating thickness in 10C-6O (16 nm) is lower than that of 32C (32 nm), the delamination rate is considerably lowered in the former. This demonstrates the role of Cr-O layer in hindering cathodic delamination. Also, a higher amount of Fe in the single step 32C sample could lead to enhanced cathodic reaction rates [9]. It was proposed previously [13] that oxides of chromium act as ohmic resistors and require quite extreme potentials for oxygen reduction reaction to occur on the surface. However, it should be emphasized that the electronic conductivity behaviour of the oxide layer would depend on the nature of the oxide film. From the results obtained in this study, it is clear that the electrodeposited metastable oxide layer performs better compared to the native chromium oxide in terms of cathodic delamination resistance. This behaviour could be related to an especially high resistance to electron transfer in these amorphous metastable layers, which leads to inhibited cathodic delamination.

The results also show that the delamination resistance of coatings with 6 nm Cr-O layer thickness is similar to that of conventional ECCS (Fig. 14b). A previous study [13] found that the delamination of single-layer Cr-O-C coatings with higher thickness and chromium oxide content was limited by the rate of electron transfer. In the present work, an increased Cr-O layer thickness has been found to result in better delamination resistance of the PVB polymer topcoat. It is obvious from the results reported here, that the actual mechanism that determines the rate of delamination, electron transfer at the delaminating interface or ion migration from anode to cathode depends sensitively on the nature of the oxide layer.

5. Conclusions

In the present study, Cr-O oxide layers of various thicknesses between 1.5 nm and 12 nm were electrodeposited on a metallic Cr-O-C layer of 10 nm thickness, from a trivalent chromium electrolyte. The coated samples were characterized using HR-TEM, APT, XPS, AES, AP-XPS and Raman Spectroscopy. The samples were coated with a model 10 wt.% PVB coating, and cathodic delamination studies were carried out. The following conclusions can be drawn:

1 As observed in TEM, no evidence for long range ordering could be found in both the chromium layers. Also, the composition profiles from APT suggest that oxygen and carbon are uniformly distributed throughout the Cr-O and Cr-O-C layers at nanoscopic scales. The APT results also revealed that the ratio of Cr:O in the Cr-O layer was found to be 1:1. The oxide in the Cr-O layer is thus deficient in oxygen, compared to the stable native oxides on chromium (Cr_2O_3 or CrOOH). The Cr:C ratio was also observed to be different from any stoichiometric carbide of chromium.
2 From the XPS data, the O1s spectrum from the surface of the Cr-O sample consisted mainly of a defective oxide or hydroxide peak. No oxide peak was observed, suggesting significantly lower reactivity to the ambient atmosphere. The O 1s spectrum from the Cr-O-C layer consisted of both the oxide and the defective oxide peaks.
3 XPS reveals the presence of carbon in a mixed organic and amorphous carbon (C = C and C–H) and carbide (Cr-C) chemical carbon states in the Cr-O-C layer and higher carbon content compared to the Cr-O layer. Raman spectra also reveal the presence of aliphatic carbon containing CH_2 and CH_3 carbon in the Cr-O-C layer and the presence of some inhomogeneity at the micrometre scale.
4 The restructuring of the Cr-O oxide phase during heat treatment was studied by *in situ* heating in 1 mbar O_2 environment in AP-XPS, from room temperature to 450 °C and Raman spectroscopy post heat treatment. The XPS profiles depicted the evolution of the oxygen-deficient or defective oxide into Cr_2O_3 oxide as the temperature was increased beyond 250 °C. This confirms the metastable nature of the Cr-O phase at ambient temperatures. Raman spectroscopy also revealed the presence of octahedrally coordinated chromium(III) as in Cr_2O_3 after heat treatment.
5 The metastable oxygen-deficient Cr-O phase was found to hinder cathodic delamination much better than the native oxide on pure chromium. This can be attributed to the resistance to electron transfer, as observed by the linear charge transfer controlled delamination kinetics. The ion migration on the surface was also inhibited on the non-stoichiometric oxide compared to the native oxide, as inferred from the shape of the delamination front.
6 The delamination resistance of the polymer topcoat was found to increase with the increase in Cr-O layer thickness. The delamination behaviour of the coating with 6 nm Cr-O layer was found to be similar to that of traditional ECCS.

Data availability

The raw/processed data required to reproduce these findings cannot be shared at this time due to legal or ethical reasons.

CRediT authorship contribution statement

J. Manoj Prabhakar: Conceptualization, Methodology, Validation, Formal analysis, Investigation, Writing - original draft, Writing - review

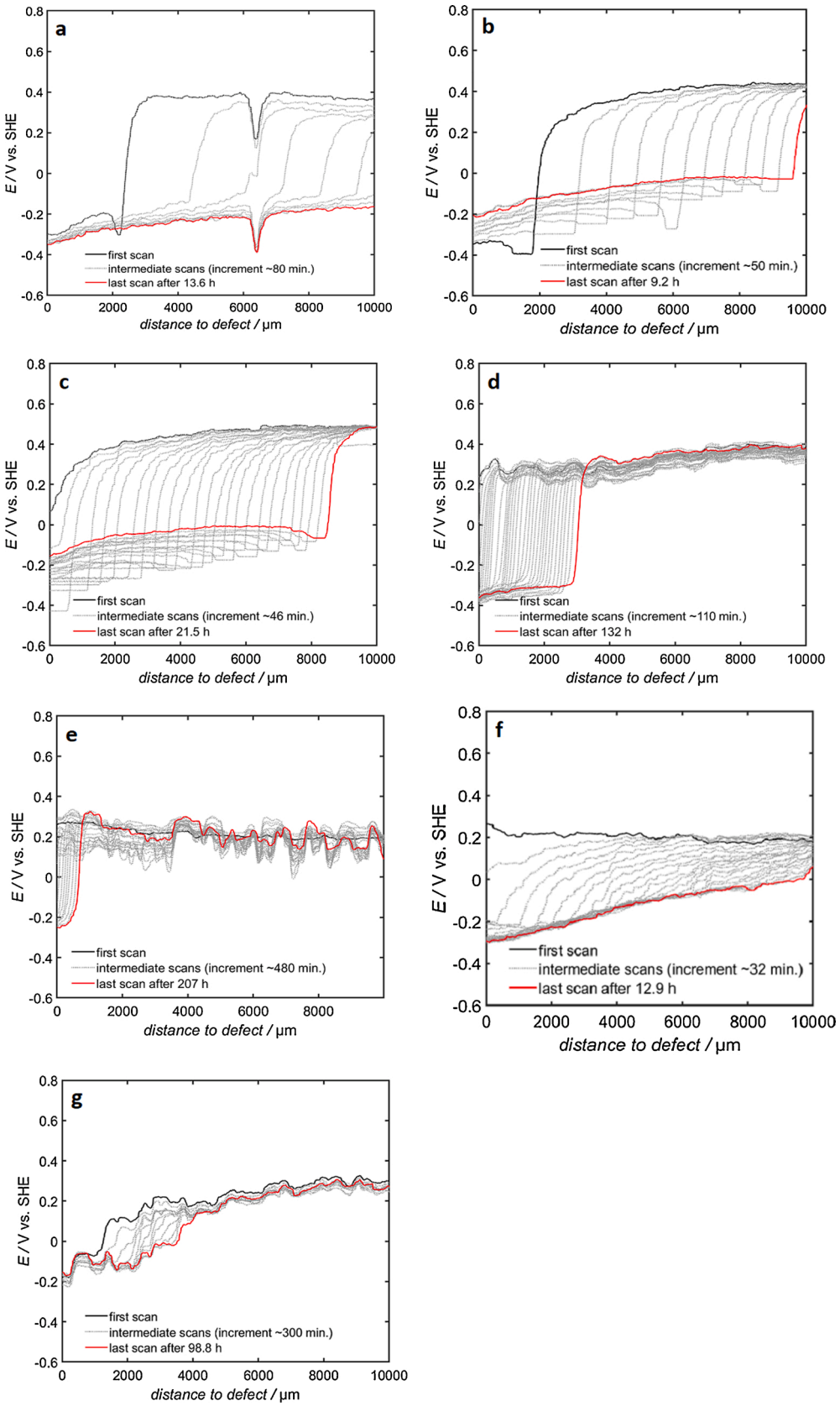

Fig. 13. Corrosion potential (E) plots as a function of distance from the defect obtained from Scanning Kelvin Probe for samples a) 32C, b) 10C-1.5O, c) 10C-3O, d) 10C-6O, e) 10C-12O, f) pure Cr with native oxide and g) ECCS.

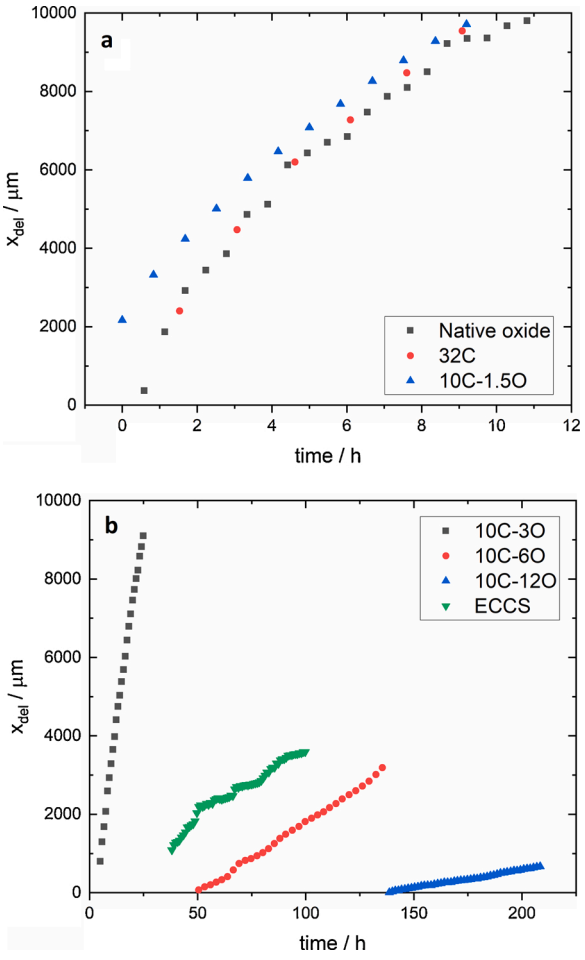

Fig. 14. Position of delamination front *vs.* time plots for samples a) 10C-1.5O, 32C and pure chromium with native oxide and b) 10C-3O, 10C-6O, 10C-12O and ECCS.

& editing, Visualization. **Rama Srinivas Varanasi:** Investigation, Formal analysis, Writing - review & editing. **Cauê Corrêa da Silva:** Investigation. **Saba:** Investigation. **Arnoud de Vooys:** Resources, Supervision. **Andreas Erbe:** Supervision, Writing - review & editing. **Michael Rohwerder:** Conceptualization, Funding acquisition, Supervision, Writing - review & editing.

Declaration of Competing Interest

The authors report no declarations of interest.

Acknowledgements

Manoj Prabhakar would like to thank Dr. Christian Liebscher and Dr. Baptiste Gault, group leaders at the MPIE, for their valuable comments and discussion on TEM and APT, respectively. Manoj Prabhakar would also like to acknowledge Dr. Koen Lammers of Tata steel, for his valuable discussions on XPS.

This work is funded by Tata Steel, Ijmuiden through IMPRS-SurMat program.

Appendix A. Supplementary data

Supplementary material related to this article can be found, in the online version, at doi:https://doi.org/10.1016/j.corsci.2021.109525.

References

[1] N.V. Mandich, D.L. Snyder, Electrodeposition of chromium. Mod. Electroplat., John Wiley & Sons, Inc., Hoboken, NJ, USA, 2011, pp. 205–248, https://doi.org/10.1002/9780470602638.ch7.
[2] T. Petry, R. Knowles, R. Meads, An analysis of the proposed REACH regulation, Regul. Toxicol. Pharmacol. 44 (2006) 24–32, https://doi.org/10.1016/j.yrtph.2005.07.007.
[3] D.J. Warren, H.N. McMurray, A.C.A. de Vooys, Localised SKP studies of cathodic disbondment on chromium/chromium oxide coated steel, ECS Trans. 50 (2013) 67–78, https://doi.org/10.1149/05047.0067ecst.
[4] N. Wint, D.J. Warren, A.C.A. DeVooys, H.N. McMurray, The use of chromium and chromium (III) oxide PVD coatings to resist the corrosion driven coating delamination of organically coated packaging steel, J. Electrochem. Soc. 167 (2020), 141506, https://doi.org/10.1149/1945-7111/abc360.
[5] S.C. Kwon, M. Kim, S.U. Park, D.Y. Kim, D. Kim, K.S. Nam, Y. Choi, Characterization of intermediate Cr-C layer fabricated by electrodeposition in hexavalent and trivalent chromium baths, Surf. Coat. Technol. 183 (2004) 151–156, https://doi.org/10.1016/j.surfcoat.2003.09.069.
[6] V.S. Protsenko, A.A. Kityk, F.I. Danilov, Kinetics and mechanism of chromium electrodeposition from methanesulfonate solutions of Cr(III) salts, Surf. Eng. Appl. Electrochem. 50 (2014) 384–389, https://doi.org/10.3103/S106837551405007X.
[7] J.H.O.J. Wijenberg, M. Steegh, M.P. Aarnts, K.R. Lammers, J.M.C. Mol, Electrodeposition of mixed chromium metal-carbide-oxide coatings from a trivalent chromium-formate electrolyte without a buffering agent, Electrochim. Acta 173 (2015) 819–826, https://doi.org/10.1016/j.electacta.2015.05.121.
[8] C. Lu, J. Lee, H. Sheu, K. Hou, C. Tseng, M. Ger, N. Defense, M.D. Section, M. Devices, Preparation and characterizations of high carbon content Cr- C coatings electroplated from a trivalent chromium-based, Int. J. Electrochem. Sci. 10 (2015) 5405–5419.
[9] N. Wint, A.C.A. de Vooys, H.N. McMurray, The corrosion of chromium based coatings for packaging steel, Electrochim. Acta 203 (2016) 326–336, https://doi.org/10.1016/j.electacta.2016.01.100.
[10] R. Giovanardi, G. Orlando, Chromium electrodeposition from Cr(III) aqueous solutions, Surf. Coat. Technol. 205 (2011) 3947–3955, https://doi.org/10.1016/j.surfcoat.2011.02.027.
[11] V. Protsenko, F. Danilov, Kinetics and mechanism of chromium electrodeposition from formate and oxalate solutions of Cr(III) compounds, Electrochim. Acta 54 (2009) 5666–5672, https://doi.org/10.1016/j.electacta.2009.04.072.
[12] J.H.O.J. Wijenberg, A.J. Wittebrood, M.W. Litz, Method For Manufacturing Chromium-Chromium Oxide Coated Blackplate, 2019. WO2019121582A1.
[13] J.E. Edy, H.N. McMurray, K.R. Lammers, A.C.A. deVooys, Kinetics of corrosion-driven cathodic disbondment on organic coated trivalent chromium metal-oxide-carbide coatings on steel, Corros. Sci. 157 (2019) 51–61, https://doi.org/10.1016/j.corsci.2019.04.037.
[14] B. Boelen, The influence of deformation on product performance of pre-coated packaging steels, 2009. http://resolver.tudelft.nl/uuid:3fa64869-991d-4a55-8708-c44cc16f8ee4.
[15] M. Stratmann, M. Wolpers, H. Streckel, R. Feser, Use of a scanning-kelvinprobe in the investigation of electrochemical reactions at the metal/polymer interface, Berichte Der Bunsengesellschaft Für Phys. Chemie. 95 (1991) 1365–1375, https://doi.org/10.1002/bbpc.19910951109.
[16] M. Stratmann, H. Streckel, R. Feser, A new technique able to measure directly the delamination of organic polymer films, Corros. Sci. 32 (1991) 467–470, https://doi.org/10.1016/0010-938X(91)90126-A.
[17] K. Hoffmann, M. Stratmann, The delamination of organic coatings from rusty steel substrates, Corros. Sci. 34 (1993) 1625–1645, https://doi.org/10.1016/0010-938X(93)90037-H.
[18] W. Fürbeth, M. Stratmann, Investigation of the delamination of polymer films from galvanized steel with the scanning Kelvinprobe, Fresenius J. Anal. Chem. 353 (1995) 337–341, https://doi.org/10.1007/BF00322064.
[19] M. Stratmann, A. Leng, W. Fürbeth, H. Streckel, H. Gehmecker, K.-H. Große-Brinkhaus, The scanning Kelvin probe; a new technique for the in situ analysis of the delamination of organic coatings, Prog. Org. Coat. 27 (1996) 261–267, https://doi.org/10.1016/0300-9440(94)00542-7.
[20] A. Leng, H. Streckel, M. Stratmann, The delamination of polymeric coatings from steel. Part 1: calibration of the Kelvinprobe and basic delamination mechanism, Corros. Sci. 41 (1998) 547–578, https://doi.org/10.1016/S0010-938X(98)00166-8.
[21] A. Leng, H. Streckel, M. Stratmann, The delamination of polymeric coatings from steel. Part 2: first stage of delamination, effect of type and concentration of cations on delamination, chemical analysis of the interface, Corros. Sci. 41 (1998) 579–597, https://doi.org/10.1016/S0010-938X(98)00167-X.
[22] A. Leng, H. Streckel, K. Hofmann, M. Stratmann, The delamination of polymeric coatings from steel part 3: effect of the oxygen partial pressure on the delamination reaction and current distribution at the metal/polymer interface, Corros. Sci. 41 (1998) 599–620, https://doi.org/10.1016/S0010-938X(98)00168-1.
[23] G.S. Frankel, M. Stratmann, M. Rohwerder, A. Michalik, B. Maier, J. Dora, M. Wicinski, Potential control under thin aqueous layers using a Kelvin probe, Corros. Sci. 49 (2007) 2021–2036, https://doi.org/10.1016/j.corsci.2006.10.017.
[24] R. Hausbrand, M. Stratmann, M. Rohwerder, The physical meaning of electrode potentials at metal surfaces and polymer/metal interfaces: consequences for delamination, J. Electrochem. Soc. 155 (2008) C369, https://doi.org/10.1149/1.2926589.
[25] M. Rohwerder, Passivity of Metals and the Kelvin Probe Technique, Elsevier Inc., 2018, https://doi.org/10.1016/B978-0-12-409547-2.13405-5.

[26] M. Rohwerder, F. Turcu, High-resolution Kelvin probe microscopy in corrosion science: scanning Kelvin probe force microscopy (SKPFM) versus classical scanning Kelvin probe (SKP), Electrochim. Acta 53 (2007) 290–299, https://doi.org/10.1016/j.electacta.2007.03.016.
[27] K. Thompson, D. Lawrence, D.J. Larson, J.D. Olson, T.F. Kelly, B. Gorman, In situ site-specific specimen preparation for atom probe tomography, Ultramicroscopy 107 (2007) 131–139, https://doi.org/10.1016/j.ultramic.2006.06.008.
[28] M. Schaffer, B. Schaffer, Q. Ramasse, Sample preparation for atomic-resolution STEM at low voltages by FIB, Ultramicroscopy 114 (2012) 62–71, https://doi.org/10.1016/j.ultramic.2012.01.005.
[29] B. Gault, M.P. Moody, J.M. Cairney, S.P. Ringer, Atom Probe Microscopy, Springer New York, New York, NY, 2012, https://doi.org/10.1007/978-1-4614-3436-8.
[30] M.K. Miller, R.G. Forbes, Atom-Probe Tomography: The Local Electrode Atom Probe, Springer U.S., Boston, MA, 2014, https://doi.org/10.1007/978-1-4899-7430-3.
[31] M.C. Biesinger, B.P. Payne, A.P. Grosvenor, L.W.M. Lau, A.R. Gerson, R.S.C. Smart, Resolving surface chemical states in XPS analysis of first row transition metals, oxides and hydroxides: Cr, Mn, Fe, Co and Ni, Appl. Surf. Sci. 257 (2011) 2717–2730, https://doi.org/10.1016/j.apsusc.2010.10.051.
[32] M.P. Moody, L.T. Stephenson, A.V. Ceguerra, S.P. Ringer, Quantitative binomial distribution analyses of nanoscale like-solute atom clustering and segregation in atom probe tomography data, Microsc. Res. Technol. 71 (2008) 542–550, https://doi.org/10.1002/jemt.20582.
[33] C.S. Pedersen, J.H. Chang, Y. Li, N. Pryds, J.M. Garcia Lastra, Phase separation in amorphous tantalum oxide from first principles, APL Mater. 8 (2020), https://doi.org/10.1063/5.0011390.
[34] L.N. Vykhodtseva, A.A. Edigaryan, E.N. Lubnin, Y.M. Polukarov, V.A. Safonov, Composition, structure, and corrosion-electrochemical properties of chromium coatings deposited from chromium(III) electrolytes containing formic acid and its derivatives, Russ. J. Electrochem. 40 (2004) 387–393, https://doi.org/10.1023/B:RUEL.0000023928.39077.6f.
[35] S. Pignataro, A. Foffani, G. Distefano, Esca study of some chromium complexes: ionization energies and multi-peak structure of the spectra, Chem. Phys. Lett. 20 (1973) 350–355, https://doi.org/10.1016/0009-2614(73)80064-8.
[36] M.C. Biesinger, B.P. Payne, L.W.M. Lau, A. Gerson, R.S.C. Smart, X-ray photoelectron spectroscopic chemical state quantification of mixed nickel metal, oxide and hydroxide systems, Surf. Interface Anal. 41 (2009) 324–332, https://doi.org/10.1002/sia.3026.
[37] E. McCafferty, J.P. Wightman, Determination of the concentration of surface hydroxyl groups on metal oxide films by a quantitative XPS method, Surf. Interface Anal. 26 (1998) 549–564, https://doi.org/10.1002/(sici)1096-9918(199807)26:8<549::aid-sia396>3.3.co;2-h.
[38] D.E. Ramaker, The past, present, and future of auger line shape analysis, Crit. Rev. Solid State Mater. Sci. 17 (1991) 211–276, https://doi.org/10.1080/10408439108243752.
[39] D.E. Ramaker, Bonding information from Auger spectroscopy, Appl. Surf. Sci. 21 (1985) 243–267, https://doi.org/10.1016/0378-5963(85)90021-2.
[40] A.M. Jubb, H.C. Allen, Vibrational spectroscopic characterization of hematite, maghemite, and magnetite thin films produced by vapor deposition, ACS Appl. Mater. Interfaces 2 (2010) 2804–2812, https://doi.org/10.1021/am1004943.
[41] M. Hanesch, Raman spectroscopy of iron oxides and (oxy)hydroxides at low laser power and possible applications in environmental magnetic studies, Geophys. J. Int. 177 (2009) 941–948, https://doi.org/10.1111/j.1365-246X.2009.04122.x.
[42] B. Lafuente, R.T. Downs, H. Yang, N. Stone, The Power of Databases: the RRUFF Project, 2016, https://doi.org/10.1515/9783110417104-003.
[43] P. Colomban, S. Cherifi, G. Despert, Raman identification of corrosion products on automotive galvanized steel sheets, J. Raman Spectrosc. 39 (2008) 881–886, https://doi.org/10.1002/jrs.1927.
[44] B.T. Sone, E. Manikandan, A. Gurib-Fakim, M. Maaza, Single-phase α-Cr2O3nanoparticles' green synthesis using Callistemon viminalis' red flower extract, Green Chem. Lett. Rev. 9 (2016) 85–90, https://doi.org/10.1080/17518253.2016.1151083.
[45] L. Li, D.Y. Kim, G.M. Swain, Transient formation of chromate in trivalent chromium process (TCP) coatings on AA2024 as probed by Raman spectroscopy, J. Electrochem. Soc. 159 (2012) C326–C333, https://doi.org/10.1149/2.019208jes.
[46] T. Yu, Z.X. Shen, J. He, W.X. Sun, S.H. Tang, J.Y. Lin, Phase control of chromium oxide in selective microregions by laser annealing, J. Appl. Phys. 93 (2003) 3951–3953, https://doi.org/10.1063/1.1558204.
[47] B.M. Weckhuysen, I.E. Wachs, R.A. Schoonheydt, Surface chemistry and spectroscopy of chromium in inorganic oxides, Chem. Rev. 96 (1996) 3327–3349, https://doi.org/10.1021/cr940044o.
[48] C. Casiraghi, A.C. Ferrari, J. Robertson, Raman spectroscopy of hydrogenated amorphous carbons, Phys. Rev. B - Condens. Matter Mater. Phys. 72 (2005) 1–14, https://doi.org/10.1103/PhysRevB.72.085401.
[49] J. Robertson, Diamond-like amorphous carbon, Mater. Sci. Eng. R Rep. 37 (2002) 129–281, https://doi.org/10.1016/s0927-796x(02)00005-0.
[50] A.C. Ferrari, Raman spectroscopy of graphene and graphite: disorder, electron–phonon coupling, doping and nonadiabatic effects, Solid State Commun. 143 (2007) 47–57, https://doi.org/10.1016/j.ssc.2007.03.052.
[51] Z. Sun, N. Dong, K. Xie, W. Xia, D. König, T.C. Nagaiah, M.D. Sánchez, P. Ebbinghaus, A. Erbe, X. Zhang, A. Ludwig, W. Schuhmann, J. Wang, M. Muhler, Nanostructured few-layer graphene with superior optical limiting properties fabricated by a catalytic steam etching process, J. Phys. Chem. C 117 (2013) 11811–11817, https://doi.org/10.1021/jp401736n.
[52] T. Tomai, Y. Kawaguchi, I. Honma, Nanographene production from platelet carbon nanofiber by supercritical fluid exfoliation, Appl. Phys. Lett. 100 (2012), 233110, https://doi.org/10.1063/1.4726113.
[53] M. Zheng, W. Du, Phase behavior, conformations, thermodynamic properties, and molecular motion of multicomponent paraffin waxes: a Raman spectroscopy study, Vib. Spectrosc. 40 (2006) 219–224, https://doi.org/10.1016/j.vibspec.2005.10.001.
[54] H.G.M. Edwards, M.J.P. Falk, Fourier-transform Raman spectroscopic study of unsaturated and saturated waxes, Spectrochim. Acta - Part A Mol. Biomol. Spectrosc. 53 (1997) 2685–2694, https://doi.org/10.1016/S1386-1425(97)00161-3.
[55] B. Prats-Mateu, M. Felhofer, A. de Juan, N. Gierlinger, Multivariate unmixing approaches on Raman images of plant cell walls: new insights or overinterpretation of results? Plant Methods 14 (2018) 1–20, https://doi.org/10.1186/s13007-018-0320-9.
[56] P. Krolop, A. Jantschke, S. Gilbricht, K. Niiranen, T. Seifert, Mineralogical imaging for characterization of the per geijer apatite iron ores in the Kiruna district, northern Sweden: a comparative study of mineral liberation analysis and raman imaging, Minerals 9 (2019) 7–11, https://doi.org/10.3390/min9090544.
[57] A.A. Edigaryan, V.A. Safonov, E.N. Lubnin, L.N. Vykhodtseva, G.E. Chusova, Y. M. Polukarov, Properties and preparation of amorphous chromium carbide electroplates, Electrochim. Acta 47 (2002) 2775–2786, https://doi.org/10.1016/S0013-4686(02)00163-9.
[58] K. Nygren, M. Samuelsson, A. Flink, H. Ljungcrantz, Å. Kassman Rudolphi, U. Jansson, Growth and characterization of chromium carbide films deposited by high rate reactive magnetron sputtering for electrical contact applications, Surf. Coat. Technol. 260 (2014) 326–334, https://doi.org/10.1016/j.surfcoat.2014.06.069.
[59] M. Andersson, J. Högström, S. Urbonaite, A. Furlan, L. Nyholm, U. Jansson, Deposition and characterization of magnetron sputtered amorphous Cr-C films, Vacuum 86 (2012) 1408–1416, https://doi.org/10.1016/j.vacuum.2012.01.021.
[60] N. Wint, A.C.A. de Vooys, H.N. McMurray, The corrosion of chromium based coatings for packaging steel, Electrochim. Acta 203 (2016) 326–336, https://doi.org/10.1016/j.electacta.2016.01.100.
[61] V. Shkirskiy, M. Uebel, A. Maltseva, G. Lefèvre, P. Volovitch, M. Rohwerder, Cathodic driven coating delamination suppressed by inhibition of cation migration along Zn|polymer interface in atmospheric CO2, Npj Mater. Degrad. 3 (2019) 1–10, https://doi.org/10.1038/s41529-018-0064-z.
[62] W. Fürbeth, M. Stratmann, The delamination of polymeric coatings from electrogalvanized steel – a mechanistic approach. Part 3: delamination kinetics and influence of CO2, Corros. Sci. 43 (2001) 243–254, https://doi.org/10.1016/S0010-938X(00)00049-4.